

Chapter 2

Methods for Testing the Non-Gaussianity of the CMB

2.1 Statistical Tests for Non-Gaussianity

2.1.1 Basic Framework

Cosmologists searching for non-Gaussianity in the CMB have to deal with two major fundamental statistical problems. First, it is not clear what to look for and which way is the best for doing that. Let us recall that non-Gaussianity—which an analyst intends to find or to rule out—can occur in various ways, since it is only defined as anything except Gaussianity (see Sect. 1.4). Therefore, there is a nearly infinite number of thinkable investigations. Besides, any analysis resulting in a non-detection of anomalous behaviour does not prove the CMB to be Gaussian, but just rules out a single type of non-Gaussianity corresponding to the characteristics of the analysis.

However, also the detection of peculiarities in the data does not immediately imply intrinsic non-Gaussianities in the microwave background, because the high amount of foreground contributions could leave hidden imprints in particular in the results of more complex analyses.

The second fundamental statistical problem of the CMB is the fact that there is only one realisation. Irrespective from foregrounds or technical difficulties, there is in theory no way to tell if a possibly detected anomalous behaviour is due to different underlying physics or just a statistical fluke. There is the idea of using the polarisation of the CMB as a new independent sample (e.g. [1–3]), however this strongly depends on the characteristics of the investigation and can not be seen as a solution in general.

The first of the two problems lead to an amazingly large amount of different measures for non-Gaussianity. A short overview over some of these measures will be given in Sect. 2.2.1. The second problem yields the fact that one has to interpret the results of the different analyses with great caution. Since any kind of possible measure is “allowed” to be used, its choice could sometimes be motivated by the characteristics of the data itself. The choice would therefore be an *a posteriori* one (cf. [4, 5]). The fact that all analyses naturally focus on anomalous features in the data, combined with a plethora of different measures used today, could lead to some

sort of preselection and therefore lowers the validity of possible anomalies. However, this does not mean that all analyses working on non-Gaussianity become redundant. In fact, every investigation claiming deviations from the theoretical properties of the microwave background is supposed to obtain a very significant result, that is in the best case confirmed by different measures. Apart from that, checks on systematics and ruling out foreground effects as a cause for the deviations is always necessary.

A common technique to search for non-Gaussianity in the microwave background is to construct simulated maps, that are Gaussian random fields which mimic the properties of the Λ CDM model. The analysis is then performed on both the data and a set of these simulations. Eventually, a comparison of the results gives information about how well the measured CMB corresponds to the theoretical demands (e.g. [6–8]). This is also accomplished in this work in Chap. 4 for the WMAP five-year data set. On the other hand, some investigations make use of particular assumptions about the nature of the non-Gaussianities by parametrising it with e.g. the non-linear coupling parameter f_{NL} (e.g. [2, 9, 10], see also below).

Clearly, both procedures depend on the model or the assumptions that are implemented. However, it might be favourable to rely on as few requirements as possible. A complementary and elegant way to investigate the non-Gaussianity of the CMB is an analysis that is completely *model-independent*. In the following Chapter, we will introduce the surrogate method, that describes one possibility of a thorough data-driven, i.e. model-independent investigation.

2.1.2 Surrogates on the Complete Sky

The concept of constructing surrogates from a given data set originates from the field of non-linear time series analysis. The basic idea was introduced in the paper of Theiler et al. [11] and subsequently applied to several different data sets, like fluid convection, sunspots, as well as electroencephalograms [12], and was continuously developed [13, 14]. Further, constrained randomisation has already been used before to generate CMB data sets with random phases as a technique for analysing the effect of cosmic strings. This was combined with a multifractal formalism in [15] for detecting cosmic string induced non-Gaussianity on synthetic CMB data sets. The surrogate method can be applied on nearly all complex systems, as outlined in [16] for the climate, stock-market and the heart-beat variability. In combination with scaling indices, which is the measure used throughout this work and will be presented in Sect. 2.2.2 below, surrogates were applied for large scale structure analysis [17] and non-Gaussianity investigations on simulated two-dimensional temperature maps [18].

The starting point for the surrogates technique is a given data set and some null hypothesis, whose validity in the data set is to be tested. The fundamental idea is then to generate surrogate data sets from the original data, which are consistent with the null hypothesis. Apart from the characteristics that are affected by the hypothesis, these surrogates share exactly the same properties as the original data set. Next, the

data as well as the surrogates are tested by means of some measure that is sensitive to characteristics, which could be induced by deviations from the null hypothesis. If different results are obtained for the original and the set of surrogates, the null hypothesis is rejected. If not, the hypothesis is confirmed.

We apply this basic concept to CMB non-Gaussianity analysis. As null hypothesis, we take the *random phase hypothesis*, which is the assumption that the phases $\phi_{\ell m}$ of the spherical harmonic coefficients $a_{\ell m}$ are independent and identically distributed in terms of a uniform distribution in the interval $[-\pi, \pi]$ (see Sect. 1.4). This assumption is on the one hand a very important and fundamental statement. Only if the random phase hypothesis holds, the construction of the power spectrum, which represents a compression of the information of a complete CMB map with several million data points to only around one thousand values, is lossless and therefore fully justified [19]. On the other hand, the statement of random phases is a direct consequence of the presumed Gaussianity of the CMB. Since the power spectrum only takes into account the linear correlations in the map, possible higher-order correlations can only be contained in the phases and the correlations among them. Thus, the presence of phase correlations would clearly disagree with Gaussianity. Any detection of inconsistencies between a CMB data set and surrogates, whose phases do not have any correlations, would therefore directly identify non-Gaussian behaviour of the CMB data. For this reason, the method of constructing surrogates used in this work is based on a phase shuffling technique, which destroys possible phase correlations of the original data set, and which is consistent with the stated null hypothesis.

Phases were already subject to analyses concerning the formation of the large scale structure in the Universe [20]. Also, a close look at the quadrupole of the CMB [21] as well as its foregrounds [22, 23] is possible in terms of a phase analysis. Investigations searching for phase correlations—and therefore non-Gaussianity—of the CMB were performed in [24–31] (see also Sect. 2.2.1 for a closer look at the results).

The method for generating surrogates by shuffling the phases is as follows: As described in detail in Sect. 1.3.3, a temperature map $T(\vec{x})$, $\vec{x} \in S$, on the complete sphere S can be expressed by means of spherical harmonics $Y_{\ell m}$,

$$T(\vec{x}) = \sum_{\ell=0}^{\ell_{\max}} \sum_{m=-\ell}^{\ell} a_{\ell m} Y_{\ell m}(\vec{x}) .$$

The sum consists of $i_{\max} = (\ell_{\max} + 1)^2$ different summands. The coefficients $a_{\ell m}$ are complex-valued, and can therefore be written in polar coordinates,

$$a_{\ell m} = |a_{\ell m}| e^{i\phi_{\ell m}} ,$$

in which the phases $\phi_{\ell m}$ can be computed as

$$\phi_{\ell m} = \arctan \frac{\text{Im}(a_{\ell m})}{\text{Re}(a_{\ell m})} .$$

To ensure that possible outliers in the data, which do not follow the assumed probability distributions as given in Sect. 1.4, are not affecting the results of the further process, one has to implement the following preprocessing. However, possible phase correlations are not affected by these two steps.

- First, the temperature values $T(\vec{x})$ are replaced by a Gaussian distribution in a rank-ordered remapping. We use the expressions $T_{old}(\vec{x})$ and $T_{new}(\vec{x})$ for denoting the temperature values before and after the remapping. Formally, we obtain:

$$T_{new}(\vec{x}_i) = D^{(k)}$$

with $D(x) \sim \mathcal{N}(\mu, \sigma)$ for $x = 1, \dots, N_{pix}$, and $D^{(1)} < D^{(2)} < \dots < D^{(N_{pix})}$. Hereby, μ and σ denote the mean and the standard deviation of $T_{old}(\vec{x})$, respectively, while k characterises the position of $T_{old}(\vec{x}_i)$ in the rank ordering

$$T_{old}^{(1)} < T_{old}^{(2)} < \dots < T_{old}^{(N_{pix})}.$$

- A similar rank ordering is applied to the values of the phases $\phi(i) = \phi_{i(\ell, m)}$:

$$\phi_{new}(i) = D^{(k)}$$

with $D(x) \sim \mathcal{U}([-\pi, \pi])$ for $x = 1, \dots, i_{max}$, and $D^{(1)} < D^{(2)} < \dots < D^{(i_{max})}$. Similar to above, k describes the position of $\phi_{old}(i)$ in the rank ordering

$$\phi_{old}^{(1)} < \phi_{old}^{(2)} < \dots < \phi_{old}^{(i_{max})}.$$

Hence, all detected deviations between the underlying map and the constructed surrogates can only be due to possible phase correlations inside the original data set.

To perform the surrogates method, one has at first to choose a shuffling interval $[\ell_1, \ell_2]$ containing the scales that are of interest in the analysis. This interval may be chosen arbitrarily inside the possible range of all multipoles, $[0, \ell_{max}]$. However, since in data maps for CMB investigations, the monopole and dipole are often subtracted, the lower bound should in this case be larger than one, $\ell_1 \geq 2$. After a convenient interval was chosen, one applies two shuffling steps onto the underlying data map, to generate two kinds of surrogates:

The first step is a shuffling of the phases of all coefficients $a_{\ell m}$, $m > 0$, outside the range $[\ell_1, \ell_2]$. In doing so, all phase correlations that correspond to scales that are not of interest, are destroyed. The resulting map with the shuffled phases is termed *first order surrogate*. The second step is to shuffle the phases of the first order surrogate inside the range of interest $[\ell_1, \ell_2]$, to create a map with no phase correlations at all. This step is to be performed multiple times to obtain several data sets. The resulting maps are denoted *second order surrogates*. In Fig. 2.1, the two phase shuffling steps are illustrated on a ℓ - m -diagram. In each step of this process, the phases with a negative m -value, $\phi_{\ell m}$, $m < 0$, have to be shuffled in the same way as the corresponding phases with the positive m -value, since otherwise the imaginary

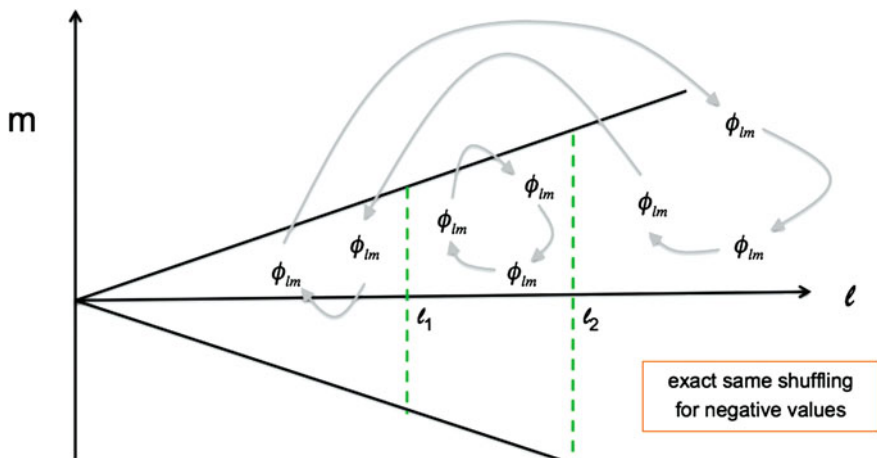


Fig. 2.1 A ℓ - m -diagram for illustration purposes of the two phase shuffling steps: At first, the phases outside $[\ell_1, \ell_2]$ are shuffled to obtain the first order surrogate, and afterwards, the phases inside the interval are shuffled multiple times to create several second order surrogates

parts of the coefficients $a_{\ell m}$ and spherical harmonics $Y_{\ell m}$ would not cancel each other. Note that all surrogates possess by definition exactly the same linear properties, that is the power spectrum, as the underlying map, since the amplitudes $|a_{\ell m}|$ were left unchanged.

The first order surrogate is then compared with the set of second order ones by means of some measure (see the following Sect. 2.2 for an overview of currently used measures in the field of CMB non-Gaussianity). Since the preprocessing steps from above ensure the correct distributions for the temperature values and the phases, any detected discrepancies have to be traced back to the phase correlations inside the first order surrogate, and are therefore a sign of non-Gaussianity *inside the chosen multipole range* of the initial map. Hence, the surrogate method presents a technique to search for deviations from Gaussianity in a range of scales which can be chosen arbitrarily.

A special case of the shuffling technique occurs if one chooses the range $[\ell_1, \ell_2] = [0, \ell_{\max}]$ (or $[\ell_1, \ell_2] = [2, \ell_{\max}]$ in case of a mono- and dipole reduced map, see above). Since this interval covers the complete range of available multipoles, generating a first order surrogate becomes dispensable. In this case, a comparison between the original map and the second order surrogates shows deviations from Gaussianity on all scales.

In Fig. 2.2, first and second order surrogates of the seven-year ILC map are illustrated with an underlying scale range of interest $[\ell_1, \ell_2] = [20, 60]$.

Despite the advantage of analyses on all arbitrary scales, the surrogates method also possesses a disadvantage: It requires a complete sphere, to ensure that the spherical harmonics are orthogonal. Otherwise, the phases of the underlying map would be coupled, which leads to induced phase correlations. For this reason, the surrogates method is performed on maps, where the foreground influences—especially those

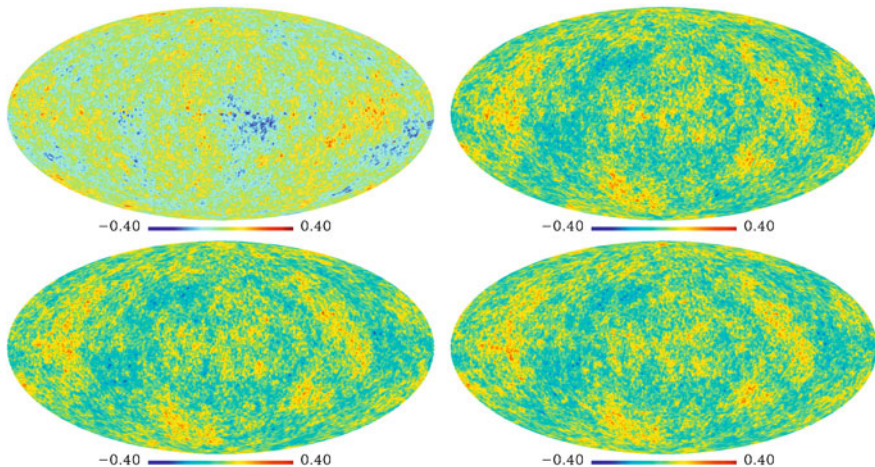


Fig. 2.2 An example of the phase shuffling method: The phases of the underlying seven-year ILC map (*upper left*) are shuffled outside the interval $[\ell_1, \ell_2] = [20, 60]$ to obtain the first order surrogate (*upper right*). Two realisations of an additional shuffling of the phases inside the interval leads to the two second order surrogates (*lower row*). Note that the structural behaviour of the large scales differs between the maps in the *upper row*, but is similar for all the first as well as the second order surrogates

due to the Galactic plane—are reduced to a minimum. This is provided by the ILC or the NILC maps (see Sect. 3.2.2). The results of these investigations are presented in Chaps. 5 and 6. But to accomplish an even more thorough analysis, it is better to mask out highly foreground affected regions like the Galactic plane, which hence puts a problem to the method. However, as a main part of this work, new ways to construct a new set of orthogonal harmonics for incomplete skies were developed, thus solving this problem. These techniques will be presented in detail in the following section, and are applied to data sets in Chap. 7.

2.1.3 Surrogates on an Incomplete Sky

The spherical harmonics form an orthonormal basis set on the complete sphere S . This statement is expressed formally by the equation

$$\int_S Y_{\ell m}(\vec{x}) Y_{\ell' m'}(\vec{x}) d\Omega = \begin{cases} 1 & \text{for } \ell = \ell' \text{ and } m = m' \\ 0 & \text{else} \end{cases} \quad (2.1)$$

where $Y_{\ell m}, Y_{\ell' m'}$ characterise two harmonic functions with $\ell, \ell' \geq 0, -\ell \leq m \leq \ell, -\ell' \leq m' \leq \ell'$. This equation describes a fundamental condition. Only if orthogonality holds, the coefficients $a_{\ell m}$ of a map $f(\vec{x})$ are unique.

If one replaces the complete sphere S in Eq. (2.1) by some incomplete sky S^{cut} , the orthogonality of the spherical harmonics obviously vanishes. This leads to severe problems, since in this case the coefficients $a_{\ell m}$ would be coupled. Hence, the random phase hypothesis no longer holds, and the surrogates technique from the previous Sect. 2.1.2 becomes inapplicable.

Incomplete skies often appear in CMB non-Gaussianity analyses: Highly foreground affected regions, in the first place the Galactic plane, strongly influence the Gaussianity of the map. Even the foreground-reduced maps, as provided by the WMAP team, still have obvious artefacts in the Galactic plane (cf. Fig. 3.4 on p. XXX). The best way to deal with this, is to apply a sky cut on these regions (cf. Sect. 3.2). The usage of full-sky maps with minimal Galactic foreground contribution, like the ILC [32] or the NILC map [33], is another solution to the problem, which avoids the sky cut. But the map-making process of these maps could induce phase correlations, which can then not be distinguished from the intrinsic higher-order correlations of the CMB.

However, there are ways to overcome this problem: In [34, 35], a method was presented, which transforms the real-valued spherical harmonics to a new set of harmonics, that is orthonormal on an user-defined cut sky. This method was improved and extended in [36]. In the present work, we adopt these techniques onto the complex-valued spherical harmonics, and combine it with the surrogates analysis, to enable investigations by surrogates on an arbitrary cut sky.

Our goal is to express any CMB temperature map

$$f(\vec{x}) = \sum_{\ell=0}^{\ell_{max}} \sum_{m=-\ell}^{\ell} a_{\ell m} Y_{\ell m}(\vec{x}), \quad \vec{x} \in S,$$

on an incomplete sky S^{cut} by means of new coefficients $a_{\ell m}^{cut}$ and new cut sky harmonics $Y_{\ell m}^{cut}: S^{cut} \rightarrow \mathbb{C}$,

$$f(\vec{x}) = \sum_{\ell=0}^{\ell_{max}} \sum_{m=-\ell}^{\ell} a_{\ell m}^{cut} Y_{\ell m}^{cut}(\vec{x}), \quad \vec{x} \in S^{cut},$$

where $Y_{\ell m}^{cut}$ is an orthogonal basis set on S^{cut} , and thus $a_{\ell m}^{cut}$ being unique.

At first, we write the spherical harmonics and the original coefficients of the underlying map, as well as the harmonics and the coefficients that we would like to obtain, into one vector each. In doing so, we only consider the modes with $m \geq 0$:

$$\begin{aligned} Y(\vec{x}) &:= [Y_{0,0}(\vec{x}), Y_{1,0}(\vec{x}), Y_{1,1}(\vec{x}), \dots, Y_{\ell_{max},\ell_{max}}(\vec{x})]^T, \\ Y^{cut}(\vec{x}) &:= [Y_{0,0}^{cut}(\vec{x}), Y_{1,0}^{cut}(\vec{x}), Y_{1,1}^{cut}(\vec{x}), \dots, Y_{\ell_{max},\ell_{max}}^{cut}(\vec{x})]^T, \\ a &:= [a_{0,0}, a_{1,0}, a_{1,1}, \dots, a_{\ell_{max},\ell_{max}}]^T \\ a^{cut} &:= [a_{0,0}^{cut}, a_{1,0}^{cut}, a_{1,1}^{cut}, \dots, a_{\ell_{max},\ell_{max}}^{cut}]^T \end{aligned}$$

All vectors have the length of $i_{max} := (\ell_{max} + 1)(\ell_{max} + 2)/2$. With the help of these terms, we can express our goal in a different way: We would like to determine two matrices $B_1, B_2 \in \mathbb{C}^{i_{max} \times i_{max}}$, that transform the vectors of the spherical harmonics and the original coefficients into the cut sky vectors of above, which is characterised formally by the following equations:

$$Y^{cut}(\vec{x}) = B_1 Y(\vec{x}) \quad (2.2)$$

$$a^{cut} = B_2 a \quad (2.3)$$

It is possible to evaluate these two matrices by applying several matrix computations onto the vector $Y(\vec{x})$. The first step, important for both the calculation of B_1 and B_2 , is the definition of the *coupling matrix* and its cut sky counterpart $C, C^{cut} \in \mathbb{C}^{i_{max} \times i_{max}}$:

$$\begin{aligned} C &:= \int_R Y(\vec{x}) Y^*(\vec{x}) d\Omega \\ C^{cut} &:= \int_R Y^{cut}(\vec{x}) (Y^{cut})^*(\vec{x}) d\Omega \end{aligned}$$

where R characterises an area on the sphere, and Y^* denotes the hermitian transposed of Y . When working with a pixelised sky, like e.g. in the HEALPix environment used for the WMAP data set, one has to replace the integral with a sum over all pixels that belong to R . The coupling matrices can be treated as positive definite for low ℓ_{max} . In addition, C and C^{cut} are hermitian by definition: For the diagonal of C , the components read as $c_{i(\ell,m),i(\ell,m)} = \int_R Y_{\ell m} \bar{Y}_{\ell m} d\Omega$, which is obviously real-valued. Outside the diagonal, we obtain $c_{i(\ell,m),i(\ell',m')} = \int_R Y_{\ell m} \bar{Y}_{\ell' m'} d\Omega = \int_R \overline{(Y_{\ell m} Y_{\ell' m'})} d\Omega = \bar{c}_{i(\ell',m'),i(\ell,m)}$. The equivalent holds for C^{cut} .

To evaluate B_1 , we have to recall the orthonormality condition (2.1) from above. Applying an adequate condition to the incomplete cut sky S^{cut} , it follows that a set of harmonics $Y_{\ell m}^{cut}$, which is orthonormal on the cut sky, needs to fulfil the equation

$$C^{cut} = I_{i_{max}}.$$

Hereby, $I_{i_{max}}$ denotes the unit matrix of size i_{max} . We can use Eq. (2.2) to change this condition to

$$B_1 C B_1^* = I_{i_{max}} \quad (2.4)$$

It is possible to decompose the coupling matrix and to calculate a matrix $A \in \mathbb{C}^{i_{max} \times i_{max}}$ which fulfills $C = A A^*$. Hereby, different matrix decomposition methods can be used, as for example the Cholesky or the eigenvalue decomposition. We will discuss this important step of the calculation in more detail below. Applying this decomposition to the above equation leads to

$$(B_1 A)(B_1 A)^* = I_{i_{max}},$$

which offers the simple solution $B_1 = A^{-1}$. Note that this does not have to be the only possible solution: In general, every matrix B_1 that fulfils Eq. (2.4) is applicable.

For B_2 , we rewrite Eq. (1.4), which offered a formula for the computation of $a_{\ell m}$, into a vectorial form,

$$a = \int_S \bar{Y}(\vec{x}) f(\vec{x}) d\Omega$$

or correspondingly

$$a^{cut} = \int_{S^{cut}} \bar{Y}^{cut}(\vec{x}) f(\vec{x}) d\Omega .$$

By inserting (2.2) and replacing the map by means of $f(\vec{x}) = a^T Y(\vec{x})$, we obtain

$$a^{cut} = \int_{S^{cut}} \bar{B}_1 (Y(\vec{x}) Y^*(\vec{x}))^T a d\Omega = \bar{B}_1 C^T a .$$

Again, we make use of the above introduced matrix decomposition and apply additionally the result of the first transformation matrix from above, $B_1 = A^{-1}$, which leads to

$$a^{cut} = \bar{B}_1 (A A^*)^T a = A^T a .$$

Thus, it follows $B_2 = A^T$.

So far, we ignored the cut sky harmonics $Y_{\ell m}^{cut}(\vec{x})$ and coefficients $a_{\ell m}^{cut}$ for $m < 0$. For their computation, we make use of Eqs. (1.5) and (1.6). We assume these equations to be valid also in the cut sky regime,

$$\begin{aligned} Y_{\ell, m}^{cut} &= (-1)^{|m|} \bar{Y}_{\ell, -m}^{cut}(x) \\ a_{\ell, m}^{cut} &= (-1)^{|m|} \bar{a}_{\ell, -m}^{cut}(x) , \end{aligned}$$

and can thus easily get the missing terms. Nevertheless, the above equations could in general lead to a non-orthogonal set of cut sky harmonics, since each $Y_{\ell, -m}^{cut}$ is by definition only orthogonal to its counterpart $Y_{\ell, m}^{cut}$, but possibly not to the rest of the harmonics. Still, for all sky cuts and ℓ -ranges that were used throughout this work, the cut sky harmonics were tested and confirmed to be orthogonal.

In summary, both transformation matrices B_1 , B_2 can be easily determined once the decomposition of the coupling matrix $C = A A^*$ was successful, and we obtain

$$Y^{cut}(\vec{x}) = A^{-1} Y(\vec{x}) \tag{2.5}$$

$$a^{cut} = A^T a . \tag{2.6}$$

However, the matrix decomposition is—from a numerical point of view—the most difficult part of the cut sky procedure, since the matrix C grows exponentially with the fourth power of ℓ_{max} . The choice of which decomposition technique one uses has a strong influence on the characteristics of the cut sky harmonics $Y_{\ell m}^{cut}$. In this work,

we will apply three different decomposition methods, the *Cholesky*, the *eigenvalue*, and the *singular value decomposition* (cf. e.g. [37]). All three techniques require the coupling matrix to be positive definite, which holds up to some ℓ_{max} that depends on the applied sky cut. The differences between the three decompositions are explained in the following.

Cholesky Decomposition

The easiest approach is the Cholesky decomposition, which was already used for the real-valued cut sky harmonics in [34] and [36]. It defines the matrix A to be lower triangular (and therefore A^* to be upper triangular), and calculates then step by step a solution for each row of A . For example, the first three diagonal elements of A have to fulfil

$$\begin{aligned}(c_{11}) &= (a_{11})^2 \\ (c_{22}) &= (a_{21})^2 + (a_{22})^2 \\ (c_{33}) &= (a_{31})^2 + (a_{32})^2 + (a_{33})^2, \dots\end{aligned}$$

which can be solved in combination with similar (but more complex) equations for the off-diagonal terms. The Cholesky decomposition is implemented in nearly every mathematical software today and provides the fastest results of all three matrix decompositions used in this work. Another advantage is the fact that A is lower triangular. Having a look at Eq.(2.6), one can see that this leads to a comfortable situation: In this case, all cut sky coefficients $a_{i^*(\ell,m)}^{cut}$ only depend on the full sky coefficients of higher multipoles, $a_{i(\ell,m)}$, $i \geq i^*$. Therefore, a monopole and dipole reduction is still possible, since these are only contained in the first four cut sky coefficients.

Eigenvalue Decomposition

Another possibility is to apply the eigenvalue decomposition, which was also used in [36] (identified there as “singular value decomposition”, which is not necessarily wrong, as we will see below). The basic idea relies on the possibility to rewrite the coupling matrix in the following way [37]:

$$C = V W V^*,$$

where the columns of V contain the eigenvectors of C , and the diagonal matrix W contains the corresponding eigenvalues. For a positive definite and hermitian C , these eigenvalues are real-valued and larger than zero, and can therefore be used to divide the above term into

$$C = V W^{1/2} (V W^{1/2})^*,$$

which leads to the solution $A = VW^{1/2}$. Hereby, $W^{1/2}$ denotes the matrix that contains the square roots of the elements of W .

Singular Value Decomposition

A method very similar to the eigenvalue decomposition is the singular value decomposition. This is based on the fact that one can write [37]

$$C = U W V^* .$$

Hereby, in contrast to above, U contains the eigenvectors of CC^* , V the eigenvectors of C^*C , and the diagonal matrix W the eigenvalues of either CC^* or C^*C , which leads to the same result. These eigenvalues are also termed *singular values* of the matrix C . Since C is hermitian, it follows $CC^* = C^*C$ and therefore $U = V$. Hence, we obtain

$$C = U W U^* = (U W^{1/2})(U W^{1/2})^*$$

and thus the result $A = U W^{1/2}$. When applying this method, it is important to consider the following: For a hermitian matrix like the used coupling matrix C , it can be shown that the resulting matrices A of eigenvector and singular value decomposition are theoretically *exactly* consistent with each other (cf. e.g. [37]). However, this does not hold in practice: The decomposition by means of the singular values yields numerically far better results than the eigenvector decomposition, since it can be applied onto larger coupling matrices (and therefore higher ℓ_{max}) and provides a faster calculation.

There exist two technical procedures that improve the decomposition processes from above:

First, the Cholesky decomposition has the advantage of a triangular transformation matrix. This does not hold for the other two decompositions, but in this case it is again possible to decompose the matrix A into a triangular matrix A' and an unitary matrix U with the same size each,

$$A = A' U ,$$

by applying a *Householder transformation*. The unitary matrix can then be ignored, since it does not change the decomposition equation $C = AA^*$, and therefore one can use A' instead of A . See the Appendix for a more detailed description of this technique.

Second, when applying a *constant latitude cut*, the majority of the terms of the coupling matrix C becomes trivial. This simplifies its calculation as well as its decomposition. See again the Appendix for more details.

Examples of the new cut sky harmonics for two different constant latitude cuts are illustrated in Fig. 2.3.

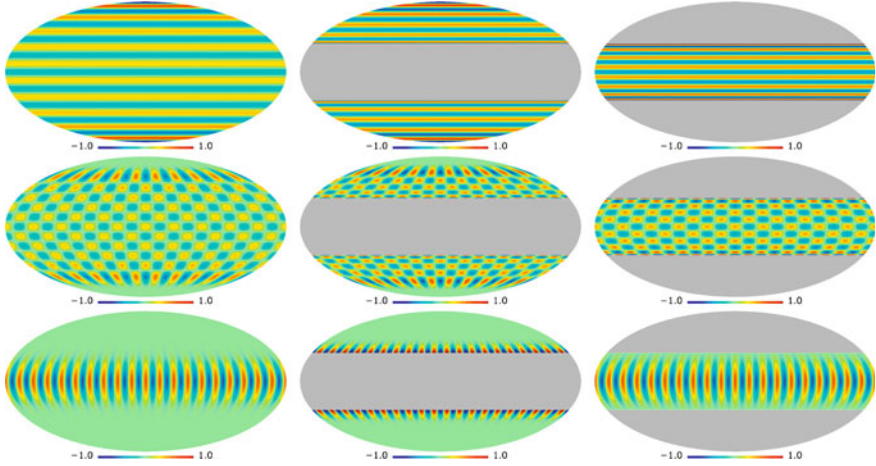


Fig. 2.3 Examples of the original spherical (*first column*) and the new cut sky harmonics for $(\ell, m) = (20, 0)$, $(20, 10)$ and $(20, 20)$ (from *top to bottom*). The harmonics were constructed by means of the singular value decomposition with additional householder transformation for $\ell_{\max} = 20$ and a constant latitude cut of $|b| < 30^\circ$ (*second column*) and $|b| \geq 30^\circ$ (*third column*), respectively. Only the real part of the complex-valued harmonics is shown in each plot

After the calculation of the new sets of cut sky harmonics $Y_{\ell m}^{\text{cut}}(\vec{x})$ and coefficients $a_{\ell m}^{\text{cut}} = |a_{\ell m}^{\text{cut}}| e^{i\phi_{\ell m}^{\text{cut}}}$ corresponding to the underlying map $f(\vec{x})$, one can finally apply the surrogates method. Similar to the previous Sect. 2.1.2, the phases

$$\phi_{\ell m}^{\text{cut}} = \arctan \frac{\text{Im}(a_{\ell m}^{\text{cut}})}{\text{Re}(a_{\ell m}^{\text{cut}})}$$

are shuffled, while the amplitudes $|a_{\ell m}^{\text{cut}}|$ are preserved. Each shuffling results in a new set of $a_{\ell m}^{\text{cut}}$'s, which corresponds to one cut sky surrogate map. Special care has to be taken when choosing the shuffling range $[\ell_1, \ell_2]$, since the scales of the structural behaviour of the map might no longer be preserved in the cut sky coefficients. For low ℓ_{\max} , a rough scale similarity still holds, though. An example of a surrogate set of the WMAP seven-year ILC map with a multipole limit of $\ell_{\max} = 40$ and a shuffling range of $[\ell_1, \ell_2] = [2, 40]$ is presented in Fig. 2.4.

But this result is not satisfying yet because of one remaining problem: By applying the cut sky transformation, the phases of the underlying data map additionally get correlated due to Eq. (2.6). This effect is shown in Fig. 2.5, which illustrates the results of a naive cut sky analysis of a simulated Gaussian CMB map with independent phases by means of scaling indices (see Sect. 2.2.2 below), for a series of increasing constant latitude cuts, that remove $|b| < 10^\circ$, $|b| < 20^\circ$ and $|b| < 30^\circ$ of the Galactic plane. The colour-coded pixels show the σ -normalised deviations between each hemisphere of the original and the surrogate data sets around this pixel. The details of this investigation are not important for the moment and will be discussed in more detail in Chap. 4. While the full sky analysis—correctly—detects no significant

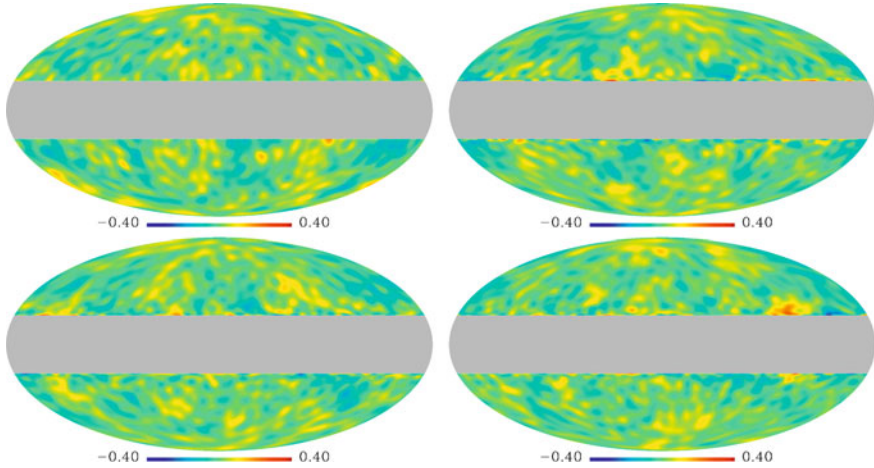


Fig. 2.4 A set of second order surrogates for the WMAP seven year ILC map (*upper left*) for a constant latitude cut, that removes $|b| < 20^\circ$ of the Galactic plane. Here, the multipole limit is $\ell_{\max} = 40$ (also for the original ILC map) and the shuffling range is chosen as $[\ell_1, \ell_2] = [2, 40]$. This represents the special case, where a shuffling outside the range is unnecessary, and therefore no first order surrogate exists

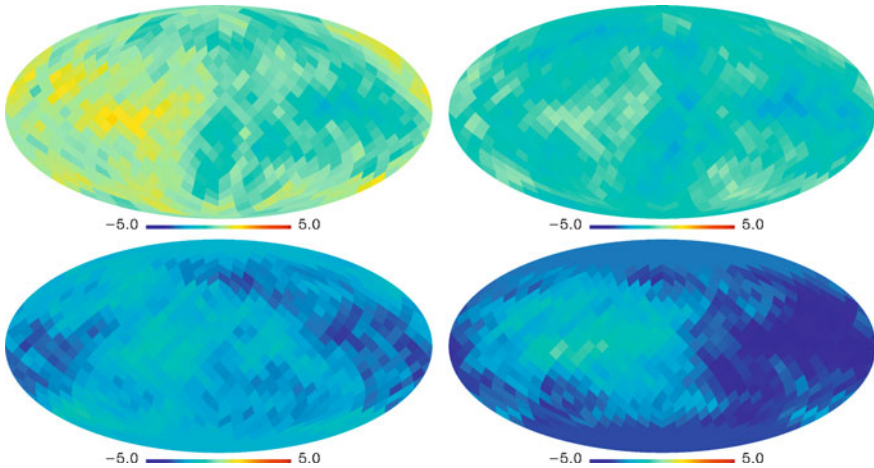


Fig. 2.5 The σ -normalised deviations between a simulated CMB map and its surrogate data sets. The colour of each pixel illustrates the mean deviation for the hemisphere around that pixel

deviations between the simulation and its surrogates, a clear shift to negative values, and therefore phase correlations, are identified for the cut sky cases. This shift is getting larger for increasing cuts, which clearly points towards a systematic effect.

A convincing analysis should therefore be able to remove these systematic effects. In Chap. 7, we will return to this problem and present an appropriate solution, thus enabling investigations by means of surrogates on an incomplete sky.

2.2 Measures for Non-Gaussianity

2.2.1 Overview Over Currently Used Measures

As soon as simulations or surrogates are created, one needs a measure being sensitive to some characteristics of the input maps and providing output values that can then be used for a comparison with the original data set. As we stated in Sect. 2.1.1, any kind of possible deviation from as well as consistency with Gaussianity marks an interesting result. Thus, one could think of a large amount of reasonable measures that could be used for the comparison. In fact, a plethora of different measures has been applied in CMB analysis until today. In general, these can be separated into *global* and *local* measures.

Global Measures

Measures of global type are related to the characteristics of the map as a whole. One of the currently most used measures is the *angular bispectrum* (e.g. [2, 9, 10]), which is the harmonic transform of the three-point correlation function. Three different configurations of the bispectrum are favoured. These depend on the shape of the triangle describing the three-point correlation function, and are termed “local” (referring to a “squeezed” triangle with two sides much larger than the third, [38]), “equilateral” [39] and “orthogonal” [40]. The result for each configuration can be expressed as one single value, the so-called *non-linear coupling parameter* f_{NL} , which describes the amount of non-Gaussianity of the primordial gravitational potential: $f_{NL} = 0$ would refer to the Gaussian case, while any larger or smaller value points towards deviations from Gaussianity. Both the parameter f_{NL} as well as the bispectrum can be used in combination with other techniques, e.g. the bispectrum with the help of the needlet coefficients (see also below), which is then referred to as *needlet bispectrum* [41–43]. Another global measure is the *power spectrum*, which we defined already on p. XXX, or the corresponding 2-point correlation function in real space. These measures were applied in [44–50]. Although the power spectrum is not a measure for non-Gaussianity (since it only analyses the Gaussian part of the temperature anisotropies, see Sect. 1.3.3), it is listed here due to the important results concerning asymmetries in the CMB sky: The power spectrum can be estimated using parts of the sky only, hence modifying it to a measure of local type, which enabled the first detection of power asymmetries in [46] (cf. Sect. 1.4). The next example for global measures are *Minkowski functionals*. These are three related measures, which can be interpreted as area, perimeter, and Euler parameter, that focus on geometrical structures in the data [9, 51]. In doing so, the map is grouped into active and inactive pixels that are defined as pixels with lower/higher values than some given threshold. Then, the structural behaviour of these two kinds of pixels is observed for different threshold values. In Chap. 7, we will use the Minkowski functionals on cut sky surrogates parallel to an analysis by means of the scaling indices, that are described in more

detail in the following Sect. 2.2.2. Similar to the Minkowski functionals, the *length of the skeleton* describes an analysis that examines the length of the zero-contour line of the map, which is defined by derivatives of the field in different directions [51]. Another two global measures are the *genus* analysis [52] and *multipole vectors* [53–59]. The former investigates the different quantities of hot and cold spots, while the latter forms a set of unit vectors, that can be used to describe and analyse a given multipole ℓ . Finally, *phase mapping techniques* are a useful tool to detect deviations of the map from a Gaussian random field [24–31]. The basic assumption for this kind of analysis—that is independent and identically distributed phases—is the same as we used above for the construction of surrogates.

Local Measures

In contrast to the global measures, local measures investigate the behaviour of the maps in a direction-dependent way. This offers the possibility to identify the position of anomalies, which can then for example be compared with a large-scale structure survey. In addition, for investigations by means of local measures, one can simply exclude heavily foreground-affected regions like the Galactic plane.

A very famous example for a local measure in CMB analysis are *wavelets*. A wavelet is a filter function, that is used to transform the underlying map into wavelet space, where the structural behaviour of the data becomes more pronounced. For CMB analysis, *directional spherical wavelets* [8, 60, 61], *steerable wavelets* [1], and *spherical mexican hat wavelets* [62–66] have been applied, in which the investigation in [62] lead to the first detection of the famous Cold Spot (cf. Sect. 1.4). A very recently developed form of wavelets are spherical *needlets*, which allow to focus on a specific set of multipoles [7, 41–43]. As already stated above, needlets can also be used to construct the needlet bispectrum.

An analysis by means of *local curvature* classifies the map points by their type of curvature, that is hills, saddles and lakes [67]. Their distribution on the sphere can then be analysed and compared to that of simulations or surrogates. Similar to the power spectrum estimation from above, some measures have in general a global behaviour, but can be used as a local one by focusing on smaller regions on the sphere. While this usage is an exception for the power spectrum, it is common for the so-called *large-angle non-Gaussianity indicators* [68–70] and the *Kolmogorov stochasticity parameter* [71–73]. The former is based on skewness and kurtosis of the temperature values inside large-angle patches of CMB maps, while the latter examines the largest difference between theoretical and empirical cumulative distribution function. The technique of considering small caps on the sphere to transform a global measure to a local one was also applied for analyses of the angular two-point correlation function in [6].

2.2.2 The Scaling Index Method

The measure for non-Gaussianity of the CMB which is applied throughout this work is the *scaling index method* (SIM) [17, 18]. This measure has the ability of revealing the topological behaviour of an input map by detecting different structures in the data, as for example cluster-like or sheet-like structures, as well as filaments or walls. While wavelets are more sensitive to structures, which offer intensity variations of significant magnitude with respect to the existing noise, scaling indices also detect structural features which possess variations within the noise level, but not significantly higher or lower intensity values [74].

Scaling indices have already been used for texture discrimination [75] and feature extraction [76, 77], time series analysis of stock exchanges [78] and active galactic nuclei [79, 80], as well as structure analysis of bone images [81] and other different medical data, like biological specimens, skin cancer, computed tomographic images, and beat-to-beat sequences from electrocardiograms [16]. Investigations concerning the Gaussianity of the CMB by applying the SIM to simulated CMB maps and the WMAP three-year data were performed in [74] and [18], respectively, where the method turned out to be of great usefulness.

The basic ideas of the SIM stem from the calculation of dimensions of strange attractors in nonlinear time series analysis. If an attractor has a non-integer dimension, it is termed *strange* [82]. These attractors play an important role in the field of dynamical systems, since systems exhibiting chaotic behaviour often possess a strange attractor in phase space [82–85]. The dimension hereby provides information about the topological characteristics of the attractor [86–88].

The basis for the calculation of the dimension of attractors from a time series is to perform a transformation of the time series into a point distribution in d -dimensional Euclidian space [89]. This transformation and the d -dimensional space are also denoted *embedding* and *embedding space*, respectively. The most common example for such an embedding are the so-called *delay-coordinates* [90]. These are constructed from a time series x_i , $i = 1, \dots, N$, of a single observed quantity from some experiment. The information of d data points can be combined to a vectors \vec{p}_i in d -dimensional Euclidian space in the following way:

$$\vec{p}_i = (x_i, x_{i+\tau}, \dots, x_{i+d\tau}) \text{ , } i \in \{1, \dots, N - d\tau\}$$

Here, the time interval τ which specifies the distance between the data points is termed delay time or lag. The resulting point set provides the analyst a completely new access for investigations of the data set. It was proven in [90], that the transformation to delay-coordinate maps is a diffeomorphism, that is a smooth invertible isomorph function with a smooth inverse that maps one differentiable manifold to another. Therefore, all the information of the time series is preserved. This result was extended to fractal sets in [89]. We use an approach analogously to this concept to enable the usage of the SIM on CMB data below.

After transforming the original data by means of such an embedding, and therefore obtaining a point set P with points \vec{p}_i , $i = 1, \dots, N_p$ in Euclidian space, one can estimate the local scaling properties of this point set. In [83], this is done by counting the number of system states around one point \vec{p}_i by means of the Heaviside function $H(x)$:

$$N(\delta, \vec{p}_i) = \sum_{j=1}^{N_p} H(\delta - \|\vec{p}_i - \vec{p}_j\|), \quad (2.7)$$

where the Heaviside function is defined as $H(x) = 1$ for $x \geq 0$ and $H(x) = 0$ else. The parameter δ is used to set a boundary: If the distance $\|\vec{p}_i - \vec{p}_j\|$ is larger than δ , the resulting $H(x)$ becomes zero. The basic idea behind the setup of Eq. (2.7) is the following fact: For small r and a large amount of points N_p , the measure behaves as a power of r , with an exponent ν [16, 83]:

$$\lim_{N_p \rightarrow \infty} \frac{1}{N_p^2} N(\delta, \vec{p}_i) \propto \delta^\nu \quad (2.8)$$

The exponent ν is again closely related to the dimensionality of the strange attractor [83, 91]. Therefore, by calculating ν , one can obtain information about the topological characteristics of the attractor. This statement is also the crucial point for the scaling index approach, as we will see below. However, due to the discontinuity of the Heaviside function, the derivate of $H(x)$, and therefore also the exponent ν , cannot be evaluated analytically. One can only approximate ν by averaging over a chosen range $[\delta_1, \delta_2]$:

$$\nu \approx \frac{\log N(\delta_2, \vec{p}_i) - \log N(\delta_1, \vec{p}_i)}{\log \delta_2 - \log \delta_1} \quad (2.9)$$

The method explained above is not the only possible approach. Similar studies were considered e.g. in [86], where a one-dimensional return map was constructed from the embedding space. From this return map, one can evaluate the characteristic exponent of the attractor. In [92], the spectrum of singularities of scaling functions is computed, in order to describe the complex scaling of the attractor.

One can now modify these ideas to apply the scaling index approach to the CMB. Here, the fluctuations of the temperature map are characterised by the values of the pixelised sky on a sphere S . Thus, the analogue of an embedding for a CMB analysis, is a transformation of the combined temperature information and the two-dimensional spatial information on the sphere into a three-dimensional point set, which includes all the information of the original map as spatial information only. Here, the pixels (θ_i, ϕ_i) , $i = 1, \dots, N_{pix}$, of S , where N_{pix} denotes the number of pixels and (θ_i, ϕ_i) latitude and longitude of the pixel i on the sphere, are converted to a point distribution in a three-dimensional space in the following way: Each temperature value $T(\theta_i, \phi_i)$ is assigned to one point \vec{p}_i , which is located in the radial direction through its pixel's centre (θ_i, ϕ_i) , that is a straight line perpendicular to the surface of the sphere. Thus,

the three-dimensional position vector of the new point \vec{p}_i reads as

$$x_i = (R + dR) \cos(\phi_i) \sin(\theta_i) \quad (2.10)$$

$$y_i = (R + dR) \sin(\phi_i) \sin(\theta_i) \quad (2.11)$$

$$z_i = (R + dR) \sin(\theta_i) \quad (2.12)$$

with

$$dR = a \left(\frac{T(\theta_i, \phi_i) - \langle T \rangle}{\sigma_T} \right), \quad (2.13)$$

where R denotes the radius of the sphere and a describes an adjustment parameter. In addition, $\langle T \rangle$ and σ_T characterise the mean and the standard deviation of the temperature fluctuations, respectively. The normalisation is performed to obtain for dR zero mean and a standard deviation of a . A transformed CMB map appearing as a three-dimensional point distribution is illustrated in Fig. 2.6. Here, two different values for a were used in the embedding process.

In general, the SIM is—like ν in Eq. (2.8)—a mapping that calculates for every point \vec{p}_i of the point set P a single value, which depends on the spatial position of \vec{p}_i in the group of the other points. P is three-dimensional for this chosen embedding of CMB data. For every point \vec{p}_i , we define the *local weighted cumulative point distribution* as

$$\rho(\vec{p}_i, r) = \sum_{j=1}^{N_{pix}} s_r(d(\vec{p}_i, \vec{p}_j))$$

with r describing the scaling range (similar to δ in Eq. (2.7)), while $s_r(\bullet)$ and $d(\bullet)$ denote a differentiable shaping function and a distance measure, respectively. To obtain the *scaling index* $\alpha(\vec{p}_i, r)$, we assume the following scaling law, which is similar to Eq. (2.8):

$$\rho(\vec{p}_i, r) \propto r^{\alpha(\vec{p}_i, r)} \quad (2.14)$$

One important difference to the above concept is the request for a differentiable shaping function $s_r(\bullet)$, which leads also to a differentiable cumulative point distribution $\rho(\vec{p}_i, r)$. Therefore, in contrast to Eq. (2.8) above, the scaling law (2.14) becomes analytically solvable. The scaling index, corresponding to the exponent ν in Eq. (2.8), can therefore be computed as the logarithmic derivative of $\rho(\vec{p}_i, r)$. If we choose e.g. Gaussian shaping functions

$$s_r(x) = e^{-\left(\frac{x}{r}\right)^n},$$

the scaling index reads as

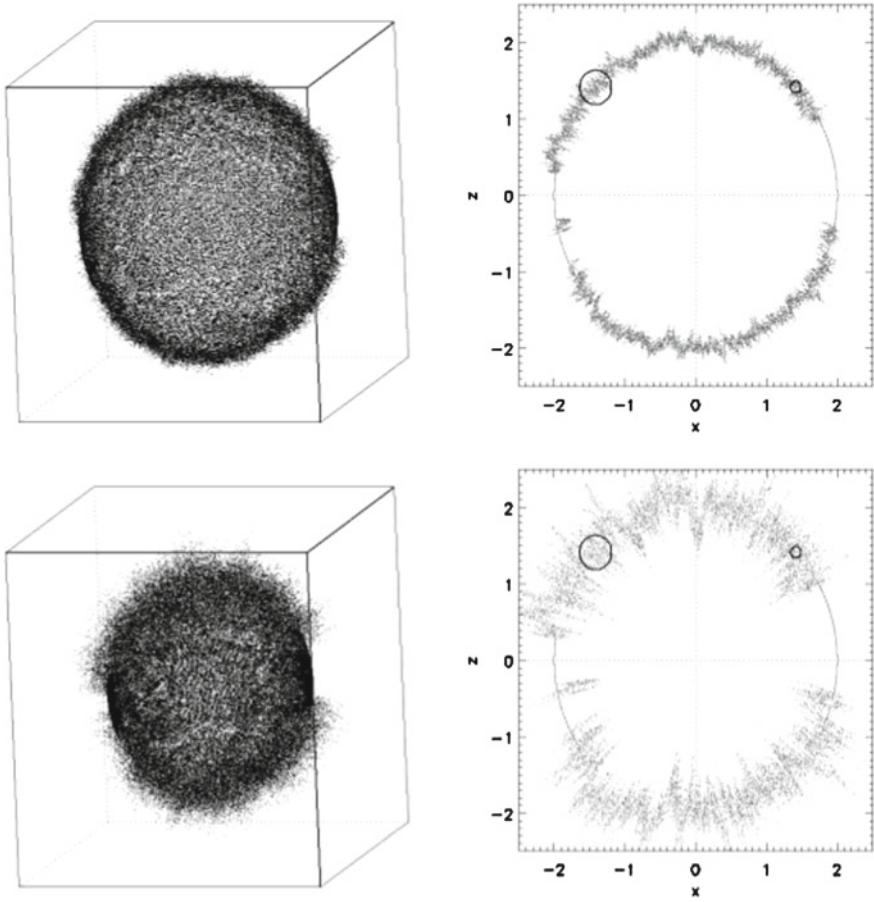


Fig. 2.6 WMAP 3-year data after application of the transformation into a three-dimensional point distribution. On the left side the full set of points is presented, while the right side shows an x, z -projection of only the points with $|y| < 0.05$. In other words, the plots show the “roughness” of the last scattering surface. Two different values for a were used, namely $a = 0.075$ (*above*) and $a = 0.225$ (*below*). The black circles represent the scaling ranges $r = 0.075$ and $r = 0.225$. Figure taken from [74]

$$\alpha(\vec{p}_i, r) = \frac{\partial \log \rho(\vec{p}_i, r)}{\partial \log r} = \frac{\sum_{j=1}^{N_{pix}} n \left(\frac{d(\vec{p}_i, \vec{p}_j)}{r} \right) e^{-\left(\frac{d(\vec{p}_i, \vec{p}_j)}{r} \right)^n}}{\sum_{j=1}^{N_{pix}} e^{-\left(\frac{d(\vec{p}_i, \vec{p}_j)}{r} \right)^n}} .$$

In general, one can freely choose $s_r(\bullet)$ and $d(\bullet)$, apart from the requirement that $s_r(\bullet)$ has to be differentiable. For the analysis in this work, we make use of a set of quadratic Gaussian shaping functions and the isotropic Euclidian norm as distance measure:

$$s_r(x) = e^{-\left(\frac{x}{r}\right)^2}$$

$$d(\vec{p}_i, \vec{p}_j) = \|\vec{p}_i - \vec{p}_j\|_2$$

Taking this into account, and using in addition the abbreviation $d_{ij} := \|\vec{p}_i - \vec{p}_j\|_2$, we obtain the final formula of the scaling indices:

$$\alpha(\vec{p}_i, r) = \frac{\sum_{j=1}^{N_{pix}} 2\left(\frac{d_{ij}}{r}\right) e^{-\left(\frac{d_{ij}}{r}\right)^2}}{\sum_{j=1}^{N_{pix}} e^{-\left(\frac{d_{ij}}{r}\right)^2}} \quad (2.15)$$

In the resulting map $\alpha(\vec{p}_i, r)$, $i = 1, \dots, N_{pix}$, the structural behaviour of the underlying point set P becomes apparent, and different types of structure can be detected very easily. The values of α are related to structural characteristics in the following way: A point- or cluster-like structure leads to scaling indices $\alpha \approx 0$, filaments to $\alpha \approx 1$ and sheet-like structures to $\alpha \approx 2$. A uniform distribution of points would result in $\alpha \approx 3$. In between, curvy lines and curvy sheets produce $1 \leq \alpha \leq 2$ and $2 \leq \alpha \leq 3$, respectively. Underdense regions in the vicinity of point-like structures, filaments or walls feature $\alpha > 3$. An example of a simulated CMB map and its scaling index response is shown in Fig. 2.7.

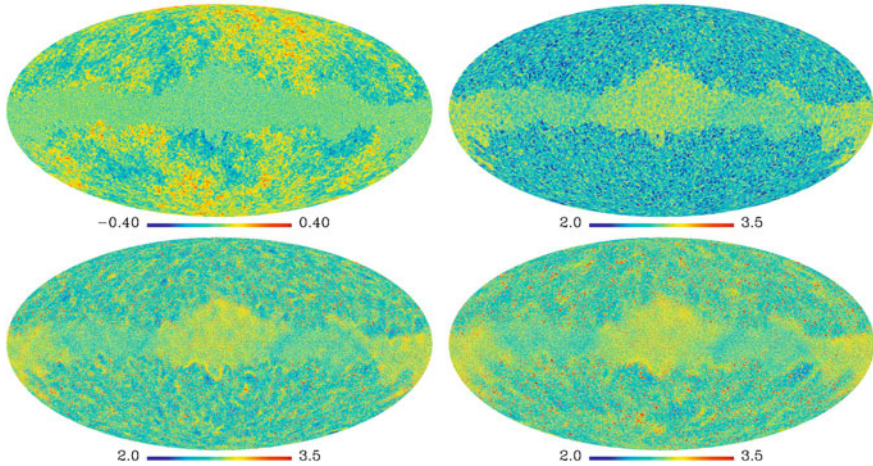


Fig. 2.7 A simulated CMB map, in which the central regions were masked out and filled with noise whose variance corresponds to the noise characteristics of the WMAP satellite (*upper left*), and the scaling index responses $\alpha(\vec{p}_i, r)$ for three different scaling ranges: $r = 0.05$ (*upper right*), $r = 0.15$ (*lower left*) and $r = 0.25$ (*lower right*). Different values of $\alpha(\vec{p}_i, r)$ correspond to different types of structure in the underlying map. Small scaling ranges examine the behaviour of the small structures, while the characteristics of the larger structure is displayed by the higher scaling ranges. Note the different structures inside and outside the masked region of the simulated map, and also the different structures in the mask itself due to the noise characteristics. Both is clearly identified by the scaling indices

From Eq. (2.15), one can see that the scaling range parameter r can be chosen arbitrarily. This parameter weights the distances between our point of interest \vec{p}_i and the remaining points \vec{p}_j (cf. definition of $s_r(x)$). Therefore, we can make use of smaller or larger values for r to examine the different behaviour of the small-scale or large-scale structural configuration in the underlying map. For the analysis in the following Chapters, we mostly make use of the ten scaling range parameters $r_k = 0.025, 0.05, \dots, 0.25, k = 1, 2, \dots, 10$. Table 4.1 on p. XXX illustrates how the positions of the resulting 90 % and 10 % weighting of the quadratic Gaussian shaping function $s_r(x)$ correspond to the angular scale ℓ in Fourier space. In Fig. 2.7, three different values of r were applied to the simulated CMB map.

In addition, both R and a from the Eqs. (2.10) and (2.13) should be chosen in a proper way to ensure a high sensitivity of the SIM with respect to the temperature fluctuations at a certain spatial scale. For CMB analysis, it turned out that this requirement is provided using $R = 2$ for the radius of the sphere and setting the parameter a , which describes the standard deviation of the normalised temperature values, to the value of the scaling range parameter r [74]. Thus, in this case the distance $1r$ corresponds to 1σ of the temperature distribution.

When we apply the scaling index method to CMB data sets, there are different methods of how to compare the results with those from simulations or surrogate maps. On the one hand, one can carry out a global analysis by calculating statistics like the mean or the standard deviation,

$$\begin{aligned} \langle \alpha_r \rangle &= \frac{1}{N_{pix}} \sum_{i=1}^{N_{pix}} \alpha(\vec{p}_i, r) \\ \sigma_{\alpha_r} &= \left(\frac{1}{N_{pix} - 1} \sum_{i=1}^{N_{pix}} [\alpha(\vec{p}_i, r) - \langle \alpha_r \rangle]^2 \right)^{1/2}, \end{aligned}$$

of the scaling index response for the complete set of pixels. On the other hand, it is also possible to perform a local analysis by focusing on a particular area, as for example a hemisphere that is located in some chosen direction on the sphere. These methods will be repeatedly applied throughout Chaps. 4–7.

References

1. P. Vielva, E. Martínez-González, M. Cruz, R.B. Barreiro, M. Tucci, *Monthly Notices of the Royal Astronomical Society*, **410**(1), 33 (2011)
2. E. Komatsu, K.M. Smith, J. Dunkley, C.L. Bennett, B. Gold, G. Hinshaw, N. Jarosik, D. Larson, M.R. Nolte, L. Page, D.N. Spergel, M. Halpern, R.S. Hill, A. Kogut, M. Limon, S.S. Meyer, N. Odegard, G.S. Tucker, J.L. Weiland, E. Wollack, E.L. Wright, *ApJS* **192**, 18 (2011)
3. D. Munshi, P. Coles, A. Cooray, A. Heavens, J. Smidt, *MNRAS* **410**, 1295 (2011)
4. E.F. Bunn, in *Proceedings of Rencontres de Moriond* (2010)

5. C.L. Bennett, R.S. Hill, G. Hinshaw, D. Larson, K.M. Smith, J. Dunkley, B. Gold, M. Halpern, N. Jarosik, A. Kogut, E. Komatsu, M. Limon, S.S. Meyer, M.R. Nolta, N. Odegard, L. Page, D.N. Spergel, G.S. Tucker, J.L. Weiland, E. Wollack, E.L. Wright, *ApJS* **192**, 17 (2011)
6. A. Bernui, *Phys. Rev. D* **78**, 063531 (2008)
7. D. Pietrobon, A. Amblard, A. Balbi, P. Cabella, A. Cooray, D. Marinucci, *Phys. Rev. D* **78**, 103504 (2008)
8. J.D. McEwen, M.P. Hobson, A.N. Lasenby, D.J. Mortlock, *MNRAS* **388**, 659 (2008)
9. E. Komatsu, A. Kogut, M.R. Nolta, C.L. Bennett, M. Halpern, G. Hinshaw, N. Jarosik, M. Limon, S.S. Meyer, L. Page, D.N. Spergel, G.S. Tucker, L. Verde, E. Wollack, E.L. Wright, *ApJS* **148**, 119 (2003)
10. K.M. Smith, L. Senatore, M. Zaldarriaga, *JCAP* **0909**, 006 (2009)
11. J. Theiler, S. Eubank, A. Longtin, B. Galdrikian, J.D. Farmer, *Physica D* **58**, 77 (1992)
12. T. Schreiber, A. Schmitz, *Physica D* **142**, 346 (2000)
13. T. Schreiber, A. Schmitz, *Phys. Rev. Lett.* **77**, 635 (1996)
14. T. Schreiber, A. Schmitz, *Phys. Rev. Lett.* **80**, 2105 (1998)
15. M.P. Pompilio, F.R. Bouchet, G. Murante, A. Provenzale, *ApJ* **449**, 1 (1995)
16. A. Bunde, J. Kropp, H.-J. Schellnhuber, *The Science of Disasters: Climate Disruptions, Heart Attacks, and Market Crashes* (Springer, Berlin, 2002)
17. C. Räth, W. Bunk, M.B. Huber, G.E. Morfill, J. Retzla, P. Schuecker, *MNRAS*, **337**, 413 (2002)
18. C. Räth, P. Schuecker, *MNRAS*, **344**, 115 (2003)
19. E. Komatsu, N. Afshordi, N. Bartolo, D. Baumann, J.R. Bond, E.I. Buchbinder, C.T. Byrnes, X. Chen, D.J.H. Chung, A. Cooray, P. Creminelli, N. Dalal, O. Dore, R. Easther, A.V. Frolov, K.M. Górski, M.G. Jackson, J. Khoury, W.H. Kinney, L. Kofman, K. Koyama, L. Leblond, J.-L. Lehnert, J.E. Lidsey, M. Liguori, E.A. Lim, A. Linde, D.H. Lyth, J. Maldacena, S. Matarrese, L. McAllister, P. McDonald, S. Mukohyama, B. Ovrut, H.V. Peiris, C. Raeth, A. Riotto, Y. Rodriguez, M. Sasaki, R. Scoccimarro, D. Seery, E. Sefusatti, U. Seljak, L. Senatore, S. Shandera, E.P.S. Shellard, E. Silverstein, A. Slosar, K.M. Smith, A.A. Starobinsky, P.J. Steinhardt, F. Takahashi, M. Tegmark, A.J. Tolley, L. Verde, B.D. Wandelt, D. Wands, S. Weinberg, M. Wyman, A.P.S. Yadav, M. Zaldarriaga, *Astro2010: The astronomy and astrophysics decadal survey*. Sci. White Pap. **158**(2009)
20. L.-Y. Chiang, P. Coles, P. Naselsky, *MNRAS* **337**, 488 (2002)
21. P.D. Naselsky, O.V. Verkhodanov, *Int. J. Mod. Phys. D* **17**, 179 (2008)
22. P. Naselsky, D. Novikov, J. Silk, *ApJ* **565**, 655 (2002)
23. P.D. Naselsky, I.D. Novikov, L.-Y. Chiang, *ApJ* **642**, 617 (2006)
24. L.-Y. Chiang, P.D. Naselsky, O.V. Verkhodanov, M.J. Way, *ApJ Lett.* **590**, L65 (2003)
25. P.D. Naselsky, A.G. Doroshkevich, O.V. Verkhodanov, *ApJ Lett.* **599**, L53 (2003)
26. P.D. Naselsky, L.-Y. Chiang, P. Olesen, O.V. Verkhodanov, *ApJ* **615**, 45 (2004)
27. P.D. Naselsky, L.-Y. Chiang, P. Olesen, I. Novikov, *Phys. Rev. D* **72**, 063512 (2005)
28. P. Coles, P. Dineen, J. Earl, D. Wright, *MNRAS* **350**, 989 (2004)
29. L.-Y. Chiang, P.D. Naselsky, *Int. J. Mod. Phys. D*, **15**, 1283 (2006)
30. L.-Y. Chiang, P.D. Naselsky, P. Coles, *ApJ* **664**, 8 (2007)
31. L.-Y. Chiang, P.D. Naselsky, *MNRAS Lett.* **380**, L71 (2007)
32. B. Gold, N. Odegard, J.L. Weiland, R.S. Hill, A. Kogut, C.L. Bennett, G. Hinshaw, X. Chen, J. Dunkley, M. Halpern, N. Jarosik, E. Komatsu, D. Larson, M. Limon, S.S. Meyer, M.R. Nolta, L. Page, K.M. Smith, D.N. Spergel, G.S. Tucker, E. Wollack, E.L. Wright, *ApJS* **192**, 15 (2011)
33. J. Delabrouille, J.-F. Cardoso, M. Le Jeune, M. Betoule, G. Fay, F. Guillaoux, *A&A* **493**, 835 (2009)
34. K.M. Górski, *ApJ Lett.* **430**, L85 (1994)
35. K.M. Górski, *ApJ Lett.* **430**, L89 (1994)
36. D.J. Mortlock, A.D. Challinor, M.P. Hobson, *MNRAS* **330**, 405 (2002)
37. W.H. Press, S.A. Teukolsky, W.T. Vetterling, B.P. Flannery, *Numerical Recipes: The Art of Scientific Computing*, 3rd edn. (Cambridge University Press, 2007)
38. D. Babich, P. Creminelli, M. Zaldarriaga, *JCAP* **0408**, 009 (2004)
39. P. Creminelli, A. Nicolis, L. Senatore, M. Tegmark, M. Zaldarriaga, *JCAP* **0605**, 004 (2006)

40. L. Senatore, K.M. Smith, M. Zaldarriaga, *JCAP* **1**, 28 (2010)
41. O. Rudjord, F.K. Hansen, X. Lan, M. Liguori, D. Marinucci, S. Matarrese, *ApJ* **701**, 369 (2009)
42. O. Rudjord, F.K. Hansen, X. Lan, M. Liguori, D. Marinucci, S. Matarrese, *ApJ* **708**, 1321 (2010)
43. P. Cabella, D. Pietrobbon, M. Veneziani, A. Balbi, R. Crittenden, G. de Gasperis, C. Quercellini, N. Vittorio, *MNRAS* **405**, 961 (2010)
44. I.J. O'Dwyer, H.K. Eriksen, B.D. Wandelt, J.B. Jewell, D.L. Larson, K.M. Górski, A.J. Banday, S. Levin, P.B. Lilje, *ApJ Lett.* **617**, L99 (2004)
45. H.K. Eriksen, G. Huey, A.J. Banday, K.M. Górski, J.B. Jewell, I.J. O'Dwyer, B.D. Wandelt, *ApJ* **665**, 1L (2007)
46. H.K. Eriksen, F.K. Hansen, A.J. Banday, K.M. Górski, P.B. Lilje, *ApJ* **605**, 14 (2004)
47. F.K. Hansen, A.J. Banday, K.M. Górski, *MNRAS* **354**, 641 (2004)
48. F.K. Hansen, A.J. Banday, K.M. Górski, H.K. Eriksen, P.B. Lilje, *ApJ* **704**, 1448 (2009)
49. J. Hoftuft, H.K. Eriksen, A.J. Banday, K.M. Górski, F.K. Hansen, P.B. Lilje, *ApJ* **699**, 985 (2009)
50. F. Paci, A. Gruppuso, F. Finelli, P. Cabella, A. De Rosa, N. Mandolesi, P. Natoli, *MNRAS* **407**, 339 (2010)
51. H.K. Eriksen, D.I. Novikov, P.B. Lilje, A.J. Banday, K.M. Górski, *ApJ* **612**, 64 (2004)
52. C.-G. Park, *MNRAS* **349**, 313 (2004)
53. D.J. Schwarz, G.D. Starkman, D. Huterer, C.J. Copi, *Phys. Rev. Lett.* **93**, 221301 (2004)
54. C.J. Copi, D. Huterer, D.J. Schwarz, G.D. Starkman, *MNRAS* **367**, 79 (2006)
55. C.J. Copi, D. Huterer, D.J. Schwarz, G.D. Starkman, *Phys. Rev. D* **75**, 023507 (2007)
56. C.J. Copi, D. Huterer, D.J. Schwarz, G.D. Starkman, *Adv. in Astr.*, 847541 (2010)
57. A. Gruppuso, C. Burigana, *JCAP* **0908**, 004 (2009)
58. A. Gruppuso, K.M. Górski, *JCAP* **03**, 019 (2010)
59. D. Sarkar, D. Huterer, C.J. Copi, G.D. Starkman, D.J. Schwarz, *Astropart. Phys.* **34**, 591 (2011)
60. J.D. McEwen, M.P. Hobson, A.N. Lasenby, D.J. Mortlock, *MNRAS* **359**, 1583 (2005)
61. J.D. McEwen, M.P. Hobson, A.N. Lasenby, D.J. Mortlock, *MNRAS Lett.* **371**, L50 (2006)
62. P. Vielva, E. Martínez-González, R.B. Barreiro, J.L. Sanz, L. Cayón, *ApJ* **609**, 22 (2004)
63. P. Mukherjee, Y. Wang, *ApJ* **613**, 51 (2004)
64. M. Cruz, E. Martínez-González, P. Vielva, L. Cayón, *MNRAS* **356**, 29 (2005)
65. M. Cruz, M. Tucci, E. Martínez-González, P. Vielva, *MNRAS* **369**, 57 (2006)
66. M. Cruz, L. Cayón, E. Martínez-González, P. Vielva, J. Jin, *ApJ* **655**, 11 (2007)
67. F.K. Hansen, P. Cabella, D. Marinucci, N. Vittorio, *ApJ Lett.* **607**, L67 (2004)
68. A. Bernui, M.J. Reboucas, *Int. J. Mod. Phys. D* **19**, 1411 (2010)
69. A. Bernui, M.J. Reboucas, A.F.F. Teixeira, *Int. J. Mod. Phys. D* **19**, 1405 (2010)
70. A. Bernui, M.J. Reboucas, *Phys. Rev. D* **81**, 063533 (2010)
71. V.G. Gurzadyan, A.A. Kocharyan, *A&A Lett.* **492**, L33 (2008)
72. V.G. Gurzadyan, A.E. Allahverdyan, T. Ghahramanyan, A.L. Kashin, H.G. Khachatryan, A.A. Kocharyan, H. Kuloghlian, S. Mirzoyan, E. Poghosian, G. Yegorian, *A&A* **497**, 343 (2009)
73. V.G. Gurzadyan, A.L. Kashin, H.G. Khachatryan, A.A. Kocharyan, E. Poghosian, D. Vetrugno, G. Yegorian, *Europhys. Lett.* **91**, 19001 (2010)
74. C. R  th, P. Schuecker, A.J. Banday, *MNRAS* **380**, 466 (2007)
75. C. R  th, G.E. Morfill, *JOSA A* **14**, 3208 (1997)
76. F. Jamitzky, R.W. Stark, W. Bunk, S. Thalhammer, C. R  th, T. Aschenbrenner, G.E. Morfill, W.M. Heckl, *Ultramicroscopy* **86**, 241 (2001)
77. C. R  th, R. Monetti, J. Bauer, I. Sidorenko, D. M  ller, M. Matsuura, E.-M. Lochm  ller, P. Zysset, F. Eckstein, *New J. Phys.* **10**, 125010 (2008)
78. R. Monetti, H. Boehm, D. M  ller, E. Rummeny, T. Link, C. R  th, *Proc. SPIE* **5370**, 215 (2004)
79. M. Gliozzi, W. Brinkmann, C. R  th, I.E. Papadakis, H. Negoro, H. Scheingraber, *A&A* **391**, 875 (2002)
80. M. Gliozzi, I.E. Papadakis, C. R  th, *A&A* **449**, 969 (2006)
81. D. M  ller, T. Link, R. Monetti, J. Bauer, H. Boehm, V. Seifert-Klauss, E. Rummeny, G. Morfill, C. R  th, *Osteo. Int.* **17**, 1483 (2006)

- 82. D. Ruelle, E. Takens, *Commun. Math. Phys.* **50**, 69 (1976)
- 83. P. Grassberger, I. Procaccia, *PRL* **50**, 346 (1983)
- 84. E.N. Lorenz, *J. Atmos. Science* **20**, 130 (1963)
- 85. E. Ott, *Rev. Mod. Phys.* **53**, 655 (1981)
- 86. N.H. Packard, J.P. Crutchfield, J.D. Farmer, R.S. Shaw, *PRL* **45**, 712 (1980)
- 87. J.C. Kaplan, J.A. Yorke, *Functional Differential Equations and Approximations of Fixed Points* (Springer, Berlin, 1979)
- 88. H. Mori, *Prog. Theor. Phys.* **63**, 1044 (1980)
- 89. T. Sauer, J.A. Yorke, M. Casdagli, *J. Stat. Phys.* **65**, 579 (1991)
- 90. F. Takens, in *Dynamical Systems and Bifurcations*, ed. by D.A. Rand, L.-S. Young. Detecting strange attractors in turbulence, *Lecture Notes in Mathematics*, vol 898, (Springer, Berlin, 1981), p. 366
- 91. P. Grassberger, R. Badii, A. Politi, *J. Stat. Phys.* **51**, 135 (1988)
- 92. T. Halsey, M.H. Jensen, L.P. Kadanoff, I. Procaccia, B.I. Shraiman, *Phys. Rev. A* **33**, 1141 (1986)

<http://www.springer.com/978-3-319-00308-5>

Non-linear Data Analysis on the Sphere
The Quest for Anomalies in the Cosmic Microwave
Background

Rossmann, G.

2013, XII, 126 p., Hardcover

ISBN: 978-3-319-00308-5